Title

Regioisomeric Engineering for Multicharge and Spin Stabilization in Two-Electron Organic Catholytes

Journal

Journal of the American Chemical Society, 147(2)

ISSN

0002-7863

Authors

Chung, HT Katie
Schramm, Tim K
Head-Gordon, Martin
et al.

Publication Date

2025-01-15

DOI

10.1021/jacs.4c16027

Peer reviewed

JACS
JOURNAL OF THE AMERICAN CHEMICAL SOCIETY
pubs.acs.org/JACS

Article

Regioisomeric Engineering for Multicharge and Spin Stabilization in Two-Electron Organic Catholytes

H. T. Katie Chung, Tim K. Schramm, Martin Head-Gordon, James Shee, and F. Dean Toste*

Cite This: *J. Am. Chem. Soc.* 2025, 147, 2115−2128

Read Online

ABSTRACT: Developing multicharge and spin stabilization strategies is fundamental to enhancing the lifetime of functional organic materials, particularly for long-term energy storage in multiredox organic redox flow batteries. Current approaches are limited to the incorporation of electronic substituents to increase or decrease the overall electron density or bulky substituents to sterically shield reactive sites. With the aim to further expand the molecular toolbox for charge and spin stabilization, we introduce regioisomerism as a scaffold-diversifying design element that considers the collective and cumulative electronic and steric contributions from all of the substituents based on their relative regioisomeric arrangements. Through a systematic study of regioisomers of near-planar aromatic cyclic triindoles and nonplanar nonaromatic cyclic tetraindoles, we demonstrate that this regioisomeric engineering strategy significantly enhances the H-cell cycling stability in the above two new classes of 2e⁻ catholytes, even when current strategies failed to stabilize the multicharged species. Density functional theory calculations reveal that the strategy operates by redistributing the charge and spin densities while highlighting the role of aromaticity in charge stabilization. The most stable 2e⁻ catholyte candidate was paired with a viologen derivative anolyte to achieve a proof-of-concept all-organic flow battery with 1.26−1.49 V, 98% capacity retention, and only 0.0117% fade/h and 0.00563% fade/cycle over 400 cycles (192 h), which is the highest capacity retention ever reported over 400 cycles in a multielectron all-organic flow battery setup. We anticipate regioisomeric engineering to be a promising strategy complementary to conventional electronic and steric approaches for multicharge and spin stabilization in other functional organic materials.

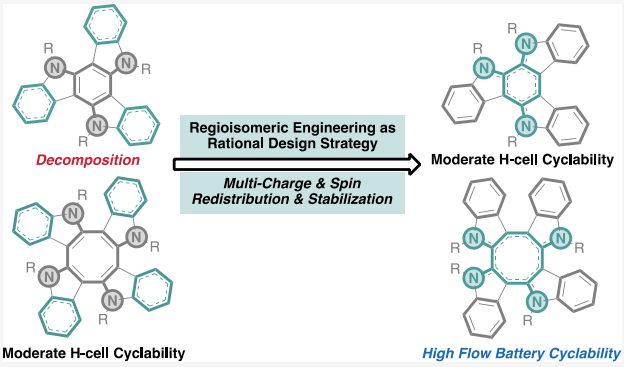

■ INTRODUCTION

Charge and spin stabilization is crucial to enhancing the performance and lifetime of functional organic materials, particularly in applications like long-term data and energy storage.[1−3] Among the various types of energy storage systems, redox flow batteries (RFBs) are a promising class of technology that enable long-term grid-scale interconversion of electrical and chemical energy. This is achieved using flowable catholytes and anolytes circulating between electrochemical cells and separated storage reservoirs.[4−7] With their capacity decoupled from power, RFBs offer engineering flexibility and economic advantages for large-scale energy storage.[7,8] Numerous single-electron (n = 1) organic catholytes[9−16] and anolytes[17−23] with high cycling stability in nonaqueous systems have been reported over the past decade. To further push the energy density limits, designing multielectron (n > 1) organic electrolytes with high cycling stability is an appealing strategy.[24−28] However, this has been a challenge from a theoretical and experimental aspect as radical and multicharged organic species are highly reactive and susceptible to decomposition.[24,27,29−32] Therefore, deconvoluting the fundamental principles of charge and spin stabilization and developing multicharge and spin stabilization strategies are imperative in guiding the design of future RFBs.

The classical strategy for thermodynamic charge and spin stabilization in π-extended systems typically involves the incorporation of electron-donating substituents or heterocycles to stabilize cationic and oxidized species[1,2,29−31,33−35] and electron-withdrawing substituents or heterocycles to stabilize anionic and reduced species (Figure 1a).[1,2,26,27,32,34,35] Alternatively, another classical strategy involves kinetic stabilization by incorporating sterically bulky groups that block reactive sites from interacting with external species that facilitate decomposition (Figure 1a).[1,2,26,27,34−36] Since most multielectron redox-active scaffolds usually consist of multiple substituents or heterocycles,[24,26,28−32] the charge and spin stabilization ability of a molecule depends on the collective and cumulative electronic and steric contributions from all the substituents based on their regioisomeric arrangements and relative

Received: November 13, 2024
Revised: December 13, 2024
Accepted: December 17, 2024
Published: January 2, 2025

https://doi.org/10.1021/jacs.4c16027
J. Am. Chem. Soc. 2025, 147, 2115−2128

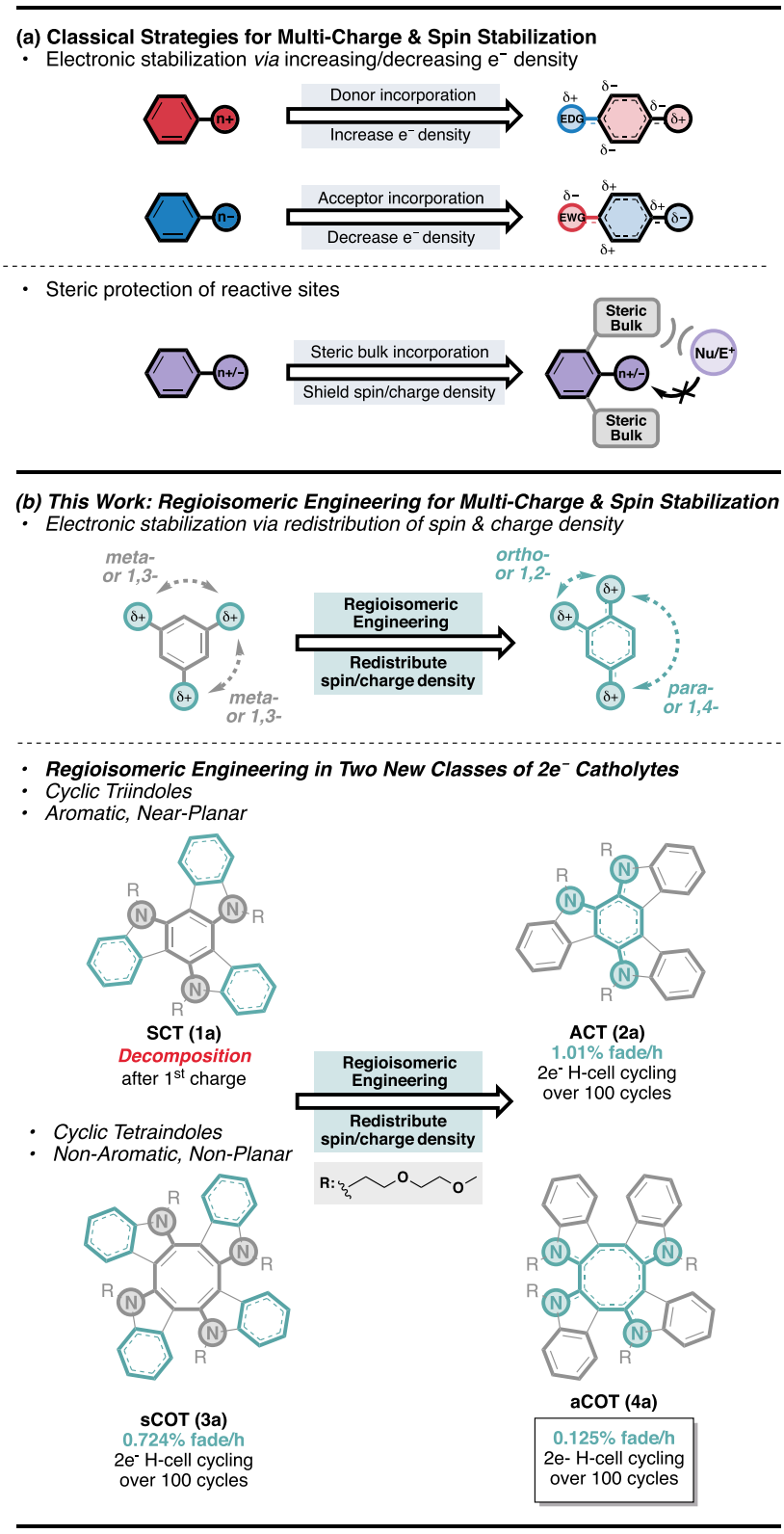

Figure 1. (a) Classical strategies for multicharge and spin stabilization in a representative 2e⁻ catholyte and 2e⁻ anolyte employed in previous studies. (b) Regioisomeric engineering for multicharge and spin stabilization in two new classes of 2e⁻ catholytes reported in this work.

orientations in a π-system. Therefore, despite being mainly studied to improve solubility in a battery context,[37−40] regioisomerism could also be engineered to achieve charge and spin stabilization and cycling stability enhancement of RBFs.

Previous structure−property studies on redox-active molecules showed that derivatives with different symmetry point groups constructed by shuffling functional groups around a π-core display drastic differences in the electrochemical stability of charged states.[41−43] However, the actual role and significance of

https://doi.org/10.1021/jacs.4c16027
J. Am. Chem. Soc. 2025, 147, 2115−2128

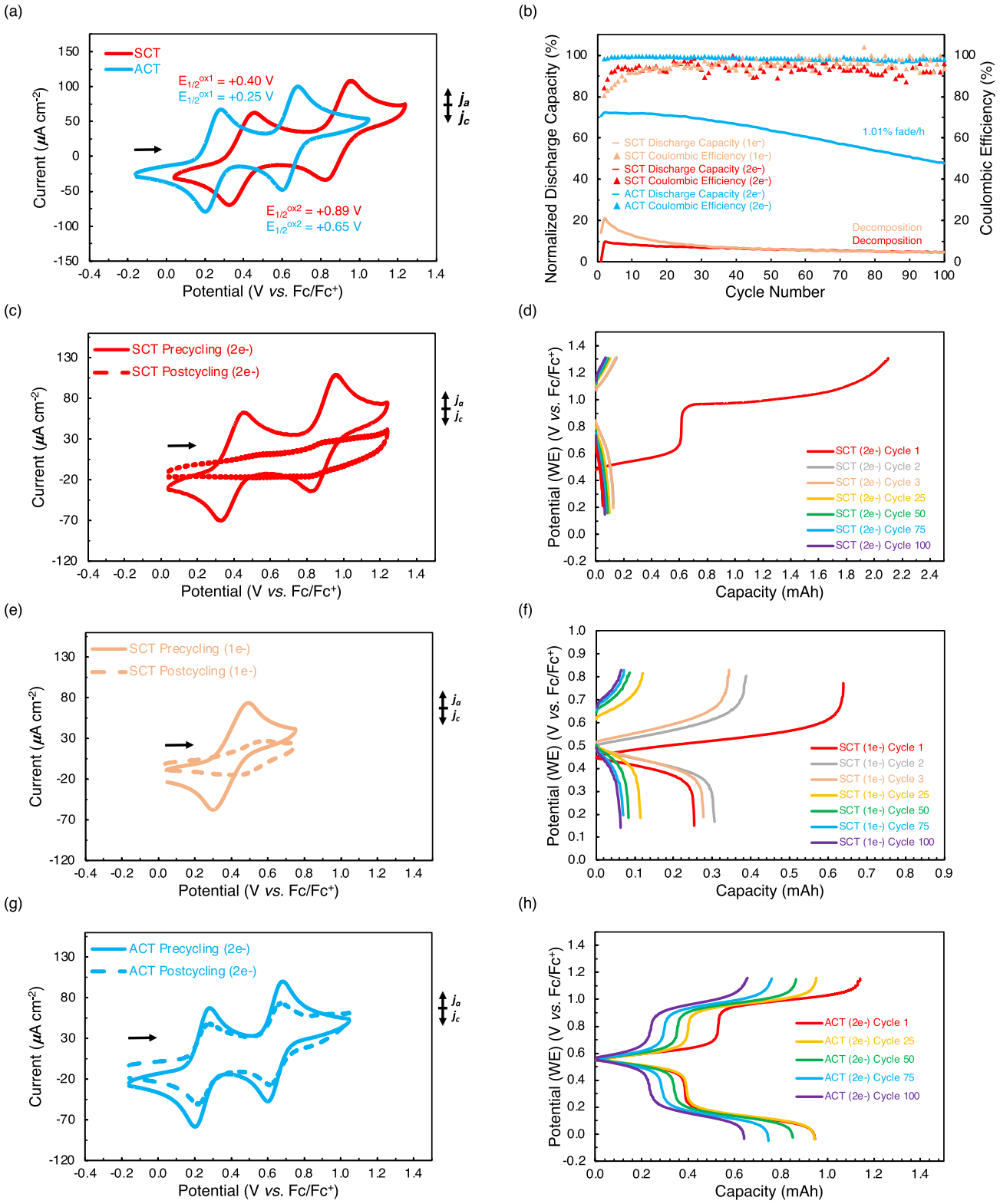

Figure 2. (a) CVs of **SCT** (**1a**) and **ACT** (**2a**). (b) Normalized discharge capacity and Coulombic efficiency versus the cycle number of 1e$^-$ H-cell cycling (pink) and 2e$^-$ H-cell cycling (red) of **SCT** (**1a**) and 2e$^-$ H-cell cycling (blue) of **ACT** (**2a**). (c) Precycling (solid line) and postcycling (dotted line) CVs of 1e$^-$ H-cell cycling of **SCT** (**1a**). (d) Potential versus capacity plots for cycles 1, 2, 3, 25, 50, 75, and 100 of 1e$^-$ H-cell cycling of **SCT** (**1a**). (e) Precycling (solid line) and postcycling (dotted line) CVs of 2e$^-$ H-cell cycling of **SCT** (**1a**). (f) Potential versus capacity plots for cycles 1, 2, 3, 25, 50, 75, and 100 of 2e$^-$ H-cell cycling of SCT (1a). (g) Precycling (solid line) and postcycling (dotted line) CVs of 2e$^-$ H-cell cycling of **ACT** (**2a**). (h) Potential versus capacity plots for cycles 1, 25, 50, 75, and 100 of 2e$^-$ H-cell cycling of **ACT** (**2a**). [CV: 5 mM catholyte, 0.5 M $TBAPF_6$/MeCN solution, scan rate = 100 mV/s, glassy carbon working electrode, Pt counter, Ag/Ag^+ (10 mM $AgBF_4$), and N_2 glovebox] H-cell cycling: 5 mM catholyte, 0.5 M $TBAPF_6$/MeCN, RVC electrodes, Ag/Ag^+ reference (10 mM $AgBF_4$/0.5 M $TBAPF_6$), 5 mA charge and discharge, for 1e$^-$ cycling: voltage cutoff = ($E_{1/2}{}^{ox1}$ ± 0.35) V; for 2e$^-$ cycling: lower voltage cutoff = ($E_{1/2}{}^{ox1}$ −0.35) V, and upper voltage cutoff = ($E_{1/2}{}^{ox2}$ + 0.35) V.

https://doi.org/10.1021/jacs.4c16027
J. Am. Chem. Soc. 2025, 147, 2115−2128

regioisomerism on the electronic structure as well as charge and spin stabilization remain either unexplored[43] or debatable, primarily due to the lack of in-depth systematic studies and the presence of multiple variables that are critical to charge and spin stabilization, such as molecular planarity[41] or charged states solubilities.[42] Therefore, deconvolution of the effect of regioisomerism on the stability of charged or radical species is essential for leveraging regioisomerism as a rational design element for spin and charge stabilization. Based on the well-known resonance effect, where ortho- or para-positions experience stronger π-donating or withdrawing effects via resonance compared to meta-positions, we hypothesize that increasing ortho- and para-resonance interactions among spin and charge stabilizing substituents increases spin and charge stabilization and hence cycling stability. This fundamental concept of charge stabilization via resonance effect has previously been used to rationalize observations such as the regioselectivities of aromatic substitution patterns,[44,45] exceptional stabilities of isolable Meisenheimer complexes,[45] and pK_a of organic acids.[46,47] Therefore, we envisioned that applying this concept, which is largely unexplored in the flow battery context, could introduce regioisomerism as a novel platform for electrolyte optimization (Figure 1b). To test this hypothesis, a systematic and comparative study of regioisomers would interrogate the differences regarding experimental galvanostatic charge−discharge cycling stabilities and provide computational descriptors that could be employed in electrolyte engineering. Aromatic near-planar cyclic triindoles[48,49] and nonaromatic nonplanar cyclic tetraindoles[50] were selected as model platforms. Both compound classes feature regioisomerism with alterable orientations of indoles, and thus, N-donor atoms around a core ring as well as synthetically accessible regioisomers[51−53] that display two well-defined oxidation peaks.[48−51] Utilizing the considerable differences in aromaticity[50,51] and conformation[50,51,53,54] between the two classes of compounds, the sensitivity of the regioisomeric engineering strategy to variations in aromaticity and geometrical distortions will also be discussed.

Herein, we report that rational regioisomeric engineering effectively enhances the experimental galvanostatic 2e$^-$ cycling stability of both the aromatic near-planar cyclic triindoles and nonaromatic nonplanar cyclic tetraindoles by increasing the ortho- (or 1,2-) and para- (or 1,4-) arrangements among charge-stabilizing indole-N donor substituents (Figure 1b). Computational insights from density functional theory (DFT) calculations revealed that the regioisomeric engineering strategy alters the charge and spin distributions in the radical cationic and dicationic states, confirming the importance of regioisomerism for charge and spin stabilization. Lastly, the asymmetrical cyclic tetraindole catholyte candidate that displays the highest H-cell cycling stability is paired with a viologen derivative and deployed in a proof-of-principle all-organic flow battery with 1.26−1.49 V, 98% capacity retention, and only 0.0117% fade/h and 0.00563% fade/cycle over 400 cycles (192 h), which is the highest capacity retention ever reported over 400 cycles in a multielectron all-organic flow battery setup.

■ RESULTS AND DISCUSSION

Multicharge and Spin Stabilization in Near-Planar Aromatic Cyclic Triindoles. Cyclic triindole has two regioisomers: high-symmetry **SCT** and low-symmetry **ACT** (Figure 1b).[48,49] In **SCT**, the indoles establish a head-to-tail linkage, resulting in a configuration where all three indole-N atoms are symmetrically distributed around the core ring in an all-meta-fashion. In contrast, in **ACT**, the orientation of one of the indoles is reversed with respect to **SCT**, yielding asymmetrically distributed indole-N atoms with ortho-, para-, and meta-arrangements. We began our studies by synthesizing **SCT** and **ACT** (see Section II of the Supporting Information), with polyethylene glycol (PEG) chains incorporated to ensure high miscibility in MeCN. The electrochemical properties of **SCT** and **ACT** were initially evaluated using cyclic voltammetry (CV) (see Section IV of Supporting Information). According to the CV data shown in Figure 2a, **SCT** showed two quasi-reversible oxidation peaks at +0.40 and +0.89 V vs the ferrocene/ferrocenium redox couple (Fc/Fc$^+$), whereas **ACT** showed two reversible oxidation peaks at +0.25 and +0.65 V vs Fc/Fc$^+$ at a scan rate of 100 mV/s. Compared to **SCT**, **ACT** exhibits a 150 and 240 mV decrease in the first and second oxidation potentials, respectively. This observation can be ascribed to the fact that symmetry lowering breaks orbital degeneracies, thereby increasing the energy of the highest occupied molecular orbital[55] (cf., Figure S37), which consequently results in slightly lower oxidation potentials in **ACT**.[49]

The CV data showed that both compounds were moderately stable on a relatively short CV time scale. However, for successful deployment in RFBs, the catholytes must exhibit long-term stability across all oxidation states. Galvanostatic H-cell 2e$^-$ charge−discharge cycling of **SCT** and **ACT** provided insights into how regioisomerism affects the long-term stability of the charged species, wherein the relative capacity fade per hour is monitored over 100 cycles (Figure 2b). Despite being electron-rich, **SCT** unexpectedly exhibited significant decomposition during the first charging event [Figure 2b (red trace)]. As shown in Figure 2d, the first oxidation during the first charging event of **SCT** occurred at around +0.40 V vs Fc/Fc$^+$ with a charging time in good agreement with the electron stoichiometry of a 1e$^-$ oxidation, indicating the formation of the radical cation **SCT**$^{\bullet+}$. However, the charging time of the second oxidation in the first charging event significantly exceeded the time required for a 1e$^-$ oxidation by more than two times. The subsequent discharge curve in the first cycle dropped rapidly with the disappearance of a two-step rereduction of the oxidized species, showing that no active material is left for discharge. This observation suggests the irreversible formation of redox-active decomposition products upon formation of the radical cation. Postcycling CV data also showed multiple new oxidation peaks at higher potentials than the second oxidation, confirming that any remaining capacity retention in the subsequent cycles is likely due to the charging and discharging of the redox-active decomposition products instead of **SCT** (Figure 2c). Data from the 1e$^-$ cycling of **SCT** showed a similar capacity fade profile [Figure 2b (pink trace) and Figure 2f] and postcycling CV features (Figure 2e), further confirming that decomposition occurred at the radical cationic state. Decomposition studies (see the Supporting Information) involving a 1e$^-$ bulk electrolysis followed by aqueous workup were conducted, and the reaction mixture was analyzed by ESI-MS. The major decomposition product was identified as arising from dimerization of two **SCT**$^{\bullet+}$ radical cations followed by deprotonation upon basic workup (Figure S1). Such a decomposition pathway is analogous to that of the related carbazole radical cations.[56,57] In stark contrast, **ACT** displays a much higher electrochemical cycling stability [Figure 2b (blue trace)] with only 1.01% capacity fade/h over 100 cycles (∼33.6 h) while cycling at approximately 62% of the theoretical capacity with ∼99%

https://doi.org/10.1021/jacs.4c16027
J. Am. Chem. Soc. 2025, 147, 2115−2128

(a) Comparison of the Excess Spin Densities of SCT-NMe•+ & ACT-NMe•+

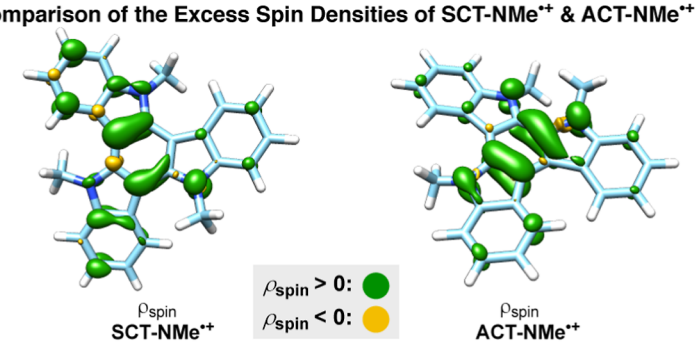

(b) Partition of Molecular Subunits for Charge and Spin Distribution Analysis

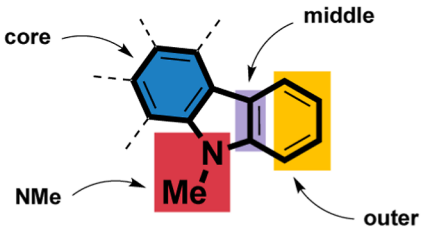

(c) Comparison of the Varying Cumulative Atomic Charge & Spin Distributions of SCT-NMe•+ & ACT-NMe•+

Δ : 0 → •+	SCT-NMe•+ spin	SCT-NMe•+ charge	SCT-NMe Δcharge	ACT-NMe•+ spin	ACT-NMe•+ charge	ACT-NMe Δcharge
outer	0.272	-0.084	+0.533	0.192	-0.080	+0.520
middle	0.108	+0.613	-0.074	0.005	+0.464	-0.118
NMe	0.201	+0.624	+0.297	0.381	+0.749	+0.361
core	0.419	-0.152	+0.244	0.422	-0.134	+0.237

(d) Application of the TCS rule to the model URFs of SCT2+ and ACT2+

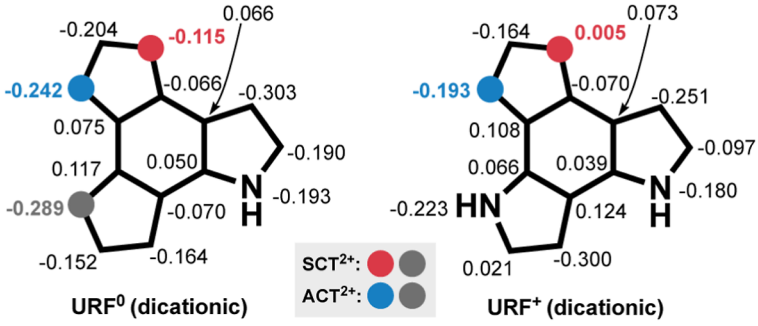

Figure 3. (a) Comparison of the excess spin density plots for the radical cations **SCT-NMe•+** and **ACT-NMe•+**. Please note that **SCT-NMe•+** is not perfectly symmetric due to slightly varying out-of-plane distortions (see Section IX of the Supporting Information). (b) Partition of molecular subunits for subsequent charge and spin distribution analysis. (c) Comparison of the varying CHELPG charge and NBO spin distributions of **SCT-NMe•+** and **ACT-NMe•+**. Δ charge represents the cumulative change in atomic CHELPG charges upon oxidation to the radical cation for the respective molecular subunit. All values result from summing over all indole units. (d) Application of the topological charge stabilization (TCS) rule to the truncated model URFs of **ACT**$^{2+}$ and **SCT**$^{2+}$. Atomic CHELPG charges of the heavy atoms are provided for the URFs corresponding to the dicationic parent species.

Coulombic efficiency, whereas **SCT** shows complete decomposition in the first charging event. Moreover, no new peak was observed in the postcycling CV of **ACT** (Figure 2g). Both plateaus in the charge−discharge curves of **ACT** (Figure 2h) occurred at the same potential over the course of the cycling experiment, resulting in the retention of around 66% of the active materials after 100 cycles. The experiments presented above provided solid experimental evidence affirming drastically enhanced stability of the radical cations and dications upon regioisomeric engineering. As the origin of this charge and spin stabilization remained elusive, we turned to DFT-based calculations, using XTB,[58] ORCA,[59] and Q-Chem,[60] for further insights.

https://doi.org/10.1021/jacs.4c16027
J. Am. Chem. Soc. 2025, 147, 2115−2128

Computational Investigation of the Origin of Multicharge and Spin Stabilization. To arrive at an accurate computational protocol for assessing the charge-stabilizing properties of the cyclic indole species, we initially conducted extensive benchmarking using the experimentally available CV data of the 12 investigated tri- and tetraindoles (see Section VIII of the Supporting Information), from which PBE0-D4 including MeCN continuum solvation emerged as the most accurate approximate density functional for this class of compounds. In addition, we established that the calculated electrochemical properties of interest were nearly invariant to the choice of PEG side-chain conformation; thus, truncated model systems with Me instead of PEG substituents were employed in all the following calculations (see the Supporting Information for a detailed discussion).

We first analyzed the charge and spin density distribution data for all species participating in the first oxidation. The spin density plots of both **SCT-NMe**$^{\bullet+}$ and **ACT-NMe**$^{\bullet+}$ (Figure 3a) reveal a substantial presence of spin density within the core benzene ring and on all nitrogen atoms. Additionally, a distinct localization pattern of excess spin on certain carbon atoms of the outer benzene rings appears for both radical cations. Please note that due to varying out-of-plane distortions, **SCT-NMe**$^{\bullet+}$ is not perfectly symmetric, which is evidently also reflected in the spin density distribution. Further, the latter is more pronounced for **SCT-NMe**$^{\bullet+}$, motivating the partition of the spin density and charge distribution into contributions from molecular subunits to quantify such apparent differences (Figure 3b,c). Going from **SCT-NMe**$^{\bullet+}$ to **ACT-NMe**$^{\bullet+}$, a significant shift of the spin density from the outer and middle carbon atoms of the peripheral benzene rings to the NMe subunits can be observed. This redistribution is also observed in the charge densities as fractional positive charge shifts from the middle carbon atoms to the NMe moieties. Additionally, the changes in atomic charges from neutral to cationic species indicate an almost entirely delocalized electron loss in both **SCT-NMe** and **ACT-NMe**. These observations are consistent for all investigated cyclic indoles (see Section X of the Supporting Information), highlighting the profound impact of regioisomeric engineering on the electronic properties of the extended π-system, notably increasing both the charge and spin density on the nitrogen atoms, which is accompanied by a stark increase in the cycling stability.

This observation of molecular stability variation based on the placement of heteroatoms within a π-conjugated system closely resembles Gimarc's rule of topological charge stabilization (TCS),[61,62] which has also recently been used by Haley and coworkers to rationalize the pronounced antiaromaticity of *s*-indacene core derivates.[63] According to the TCS rule, the thermodynamic stability of a heterocyclic system is increased when electronegative heteroatoms occupy positions characterized by sizable negative charge densities, as obtained from population analysis on iso-π-electronic hydrocarbon uniform reference frames without said heteroatoms.[61,62] Two truncated URFs of interest, corresponding to the dicationic triindoles, are shown in Figure 3d, where the total charge of the reference systems has been reduced by one for each nitrogen atom substituted with a carbon atom in order to preserve the total number of π-electrons. In both cases, the computed atomic charges indicate a clear preference for the asymmetric placement of electronegative nitrogen atoms (blue). However, caution is warranted for a general, straightforward application of the TCS rule due to difficulties arising from significant deviations from ideal planarity of the extended molecules; thus, truncated URFs with greater planarity were employed herein. We also note that the influence of molecular topology on charge stabilization is most prominent in highly charged species, as confirmed by our calculations on URFs with varying reference oxidation states (please refer to Section XIII of the Supporting Information for a detailed discussion of these results and more details on applying the TCS rule). Despite minor inconsistencies, our TCS analysis reinforced previous findings on the charge and spin distributions by suggesting that the arrangement of heteroatoms in **ACT-NMe**, leading to enhanced charge stabilization, is also favored based on the molecular topology of the system, thus facilitating improved conjugation.

We now proceeded to computationally investigate the potential decomposition pathways inherent to the radical cationic species. N-substituted carbazoles are known to undergo radical dimerization para to the N-donor group (C5, Figure 3b).[56,57] However, the spin density localization patterns from Figure 3a imply an electronic preference for radical dimerization at the C4 and C6 positions using the peripheral numbering of indole (Figure 3b). This is further supported by radical Fukui function calculations[64] (Figure S50). Evidently, positions C4 and C7 are more sterically hindered (Table S39); thus, only the 5,5′- and 6,6′-dimers that result from connecting the corresponding carbon atoms with maximal local spin density were investigated. Figure S53 shows the free-energy profile for the proposed radical recombination of **SCT-NMe**$^{\bullet+}$ and **ACT-NMe**$^{\bullet+}$, followed by deprotonation-facilitated rearomatization to the corresponding σ-dimers. In line with the electronic positional preference, the calculated dimerization barriers are consistently higher for the 5,5′-dimers. Most interestingly, the 6,6′-dimerization barrier for **SCT-NMe**$^{\bullet+}$ was the lowest calculated. Combined with the calculated energetics of the **4F-ACT-NMe**$^{\bullet+}$ dimer (see Table S40), the barriers for the 6,6′-dimerization thus align qualitatively with the electrochemical stabilities observed experimentally, suggesting 6,6′-dimerization to be a critical initial step of the decomposition mechanism. Nevertheless, a quantitative relationship between the local spin densities as well as other tested molecular descriptors with the experimental fade rates could not be established (see Section XVI of the Supporting Information for details).

In summary, the DFT calculations suggest the origin of charge and spin stabilization through regioisomeric engineering to be a significant redistribution of the charge and spin density. Increased heteroatom participation reduces the availability of spin density on peripheral carbon atoms of the asymmetric trimers, consequently raising dimerization barriers, with the 6,6′-barrier still being the most favorable.

Comparison with Classical Strategies. To compare the effectiveness of regioisomeric engineering with classical strategies of incorporation of electron-donating groups and sterically bulky groups in multispin and charge stabilization, **5OMe-SCT** and **5Me-SCT** were synthesized and electrochemically evaluated, respectively [Figure S2(1,2)]. The CV of **5OMe-SCT** displayed two quasi-reversible oxidations peaks at +0.30 and +0.72 V vs Fc/Fc$^+$, while **5Me-SCT** displayed two reversible oxidations peaks at +0.33 and +0.82 V vs Fc/Fc$^+$ at a scan rate of 100 mV/s. For the H-cell cycling experiments, both **5OMe-SCT** and **5Me-SCT** displayed decomposition after the first charge in the 2e$^-$ H-cell cycling studies. Charge−discharge curves and postcycling CVs also confirmed the complete decomposition of the active species after 100 cycles. Therefore, these results highlight that redistributing electron densities upon

https://doi.org/10.1021/jacs.4c16027
J. Am. Chem. Soc. 2025, 147, 2115−2128

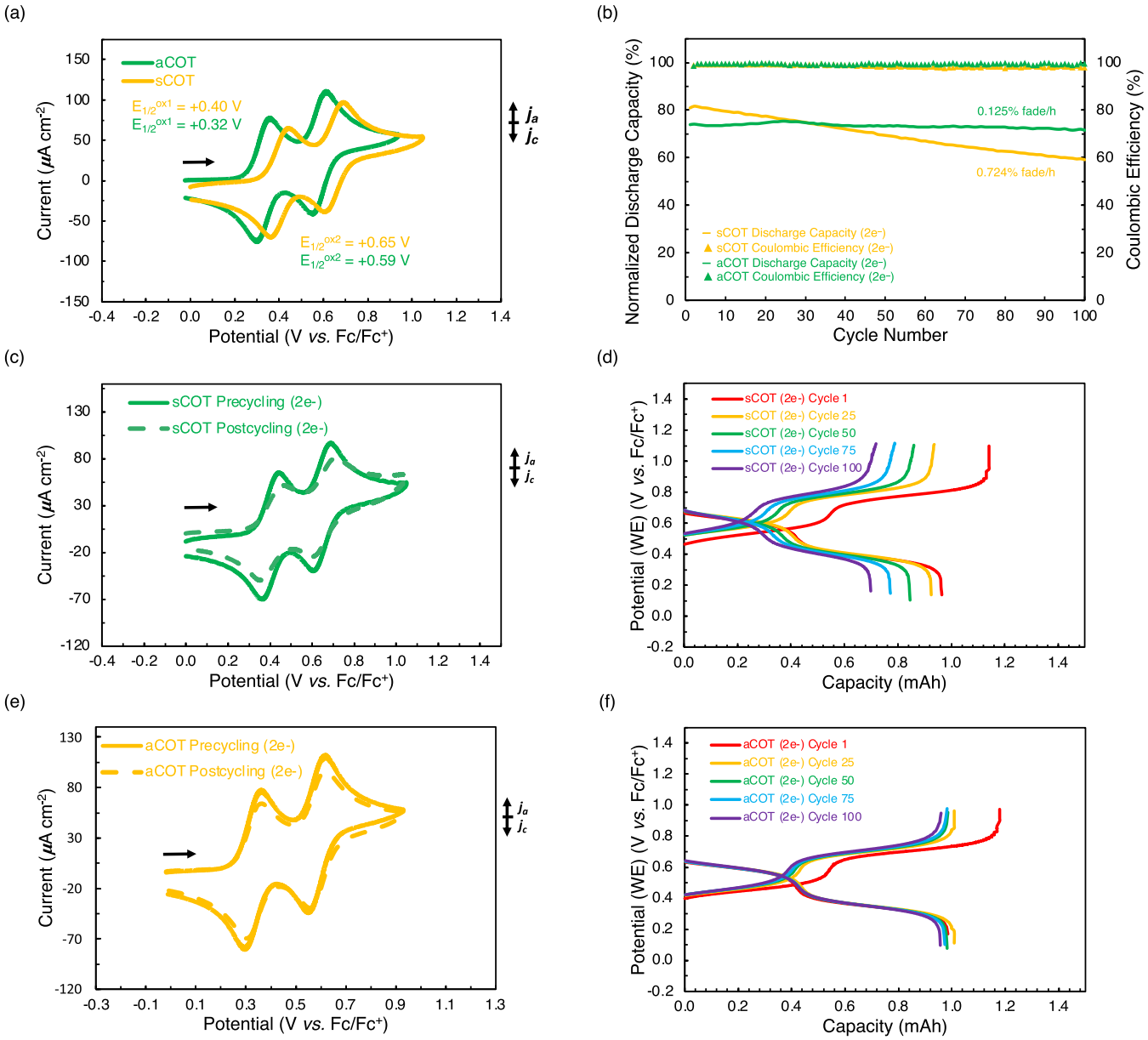

Figure 4. (a) CVs of **sCOT** (**3a**) and **aCOT** (**4a**). (b) Normalized discharge capacity and Coulombic efficiency versus the cycle number of 2e⁻ H-cell cyclings of **sCOT** (**3a**) (yellow) and **aCOT** (**4a**) (green). (c) Precycling (solid line) and postcycling (dotted line) CVs of 2e⁻ H-cell cycling of **sCOT** (**3a**). (d) Potential versus capacity plots for cycles 1, 25, 50, 75, and 100 of 2e⁻ H-cell cycling of **sCOT** (**3a**). (e) Precycling (solid line) and postcycling (dotted line) CVs of 2e⁻ H-cell cycling of **aCOT** (**4a**). (f) Potential versus capacity for cycles 1, 25, 50, 75, and 100 of 2e⁻ H-cell cycling of **aCOT** (**4a**) (CV: 5 mM catholyte, 0.5 M $TBAPF_6$/MeCN solution, scan rate = 100 mV/s, glassy carbon working electrode, Pt counter, Ag/Ag^+ (10 mM $AgBF_4$), and N_2 glovebox) (H-cell cycling: 5 mM catholyte, 0.5 M $TBAPF_6$/MeCN, RVC electrodes, Ag/Ag^+ reference (10 mM $AgBF_4$/0.5 M $TBAPF_6$), 5 mA charge and discharge, lower voltage cutoff = ($E_{1/2}^{ox1}$ −0.35) V, and upper voltage cutoff = ($E_{1/2}^{ox2}$ + 0.35) V).

regioisomeric engineering is equally or even more effective in multispin and charge stabilization than simply increasing (or decreasing) or shielding electron densities enabled by classical strategies.

Multicharge and Spin Stabilization in Nonplanar Nonaromatic Cyclic Tetraindoles. Since regioisomeric engineering is based on π-resonance stabilization interactions, the strategy is expected to be sensitive to geometrical distortions of the conjugated system. Hence, the effectiveness of the strategy was further probed by application to nonplanar species. Cyclic tetraindoles (Figure 1b), a class of compounds with one additional indole unit compared to the cyclic triindoles, are good candidates for this study as they feature an 8π nonaromatic tub-shaped cyclooctatetraene (COT) core, tunable regioisomerism around the core ring, and two oxidation waves in MeCN.[50] Utilizing the considerable differences in aromaticity between the aromatic cyclic triindoles and nonaromatic cyclic tetraindoles,[50,51] the effect of aromaticity on the electrochemistry and its interplay with regioisomerism on charge and spin stabilization can also be studied. Among the four regioisomers of cyclic tetraindoles formed upon altering the orientations of the indole units (Figure S32), **sCOT** and **aCOT** (PEG chains were incorporated to ensure high miscibility in MeCN) are the two most synthetically accessible ones based on previous literature.[50,51,53,54]

https://doi.org/10.1021/jacs.4c16027
J. Am. Chem. Soc. 2025, 147, 2115−2128

(a) Comparison of the Excess Spin Densities of sCOT-NMe•+ & aCOT-NMe•+

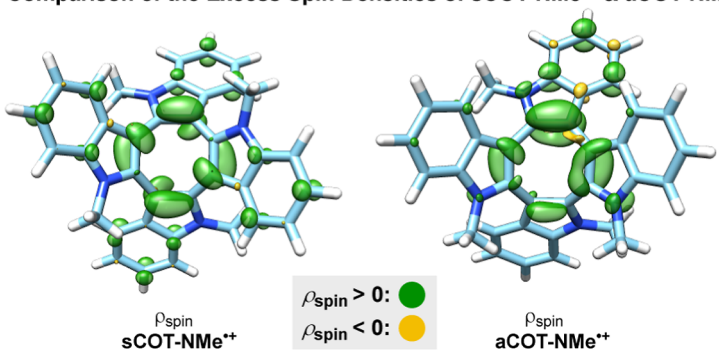

(b) Comparison of the Varying Cumulative Atomic Charge & Spin Distributions of sCOT-NMe•+ & aCOT-NMe•+

	sCOT-NMe•+	sCOT-NMe•+	sCOT-NMe	aCOT-NMe•+	aCOT-NMe•+	aCOT-NMe
Δ : 0 → •+	spin	charge	Δcharge	spin	charge	Δcharge
outer	0.233	-0.281	+0.485	0.196	-0.259	+0.491
middle	0.063	+0.714	+0.160	0.038	+0.602	+0.112
NMe	0.008	+0.712	-0.045	0.092	+0.862	+0.059
core	0.696	-0.145	+0.400	0.674	-0.206	+0.339

(c) Application of the TCS rule to the model URFs of sCOT2+ and aCOT2+

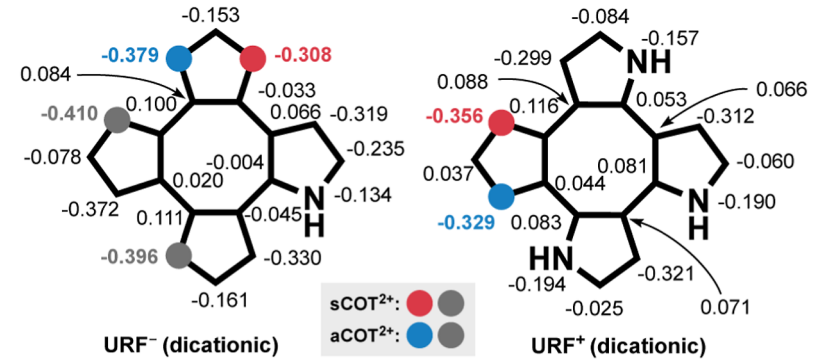

Figure 5. (a) Comparison of the excess spin density plots for the radical cations **sCOT-NMe**$^{\bullet+}$ and **aCOT-NMe**$^{\bullet+}$. (b) Comparison of the varying CHELPG charge and NBO spin distributions of **sCOT-NMe**$^{\bullet+}$ and **aCOT-NMe**$^{\bullet+}$. Δ charge represents the cumulative change in atomic CHELPG charges upon oxidation to the radical cation for the respective molecular subunit. All values result from summing over all indole units. (c) Application of the TCS rule to the truncated model URFs of **sCOT**$^{2+}$ and **aCOT**$^{2+}$. Atomic CHELPG charges of the heavy atoms are provided for the URFs corresponding to the dicationic parent species, indicating a smaller influence of molecular topology on charge stabilization for the tetraindoles compared to the triindoles.

Compounds **sCOT** and **aCOT** were first synthesized (see Section II of the Supporting Information) and electrochemically assessed using experiments similar to those employed for **SCT** and **ACT** (see Section IV of the Supporting Information). At a scan rate of 100 mV/s, the CV of **sCOT** [Figure 4a (yellow trace)] showed two reversible oxidation peaks at +0.40 and +0.65 V vs Fc/Fc$^+$, while the CV of **aCOT** [Figure 4a (green trace)] featured two reversible oxidation peaks at +0.32 and +0.59 V vs Fc/Fc$^+$. Compared to **sCOT**, **aCOT** has an 80 and 60 mV decrease in the first and second oxidation potentials, respectively, as is again expected for breaking orbital degeneracies.[55]

Moreover, the differences between the first and second oxidation potentials in the triindoles (490 mV for **SCT** and 400 mV for **ACT**) are more significant compared to that of the tetraindoles (250 mV for **sCOT** and 270 mV for **aCOT**). The proposed reason is a drastic decrease in aromaticity upon oxidation in the triindoles, which necessitates a more significant thermodynamic driving force in the form of higher oxidation potentials to access the dicationic states. In comparison, the reduction in aromaticity upon oxidation is less pronounced for the tetraindoles,[50,51] thus requiring a smaller thermodynamic driving force with lower oxidation potentials to access the dicationic states. These changes in aromatic character upon oxidation were deduced from magnetic (nucleus-independent chemical shieldings[65−68]), geometric (harmonic oscillator model of aromaticity),[69,70] and electron delocalization-based (aromatic fluctuation index[71,72]) aromaticity descriptors, as detailed in Section XII of the Supporting Information. In summary, the calculations suggest negligible changes in

https://doi.org/10.1021/jacs.4c16027
J. Am. Chem. Soc. 2025, 147, 2115−2128

aromaticity for all outer benzene units, while a consistent decrease in aromaticity is observed for the pyrrole rings of the investigated species. As expected, the aromaticity of the core ring in the triindoles significantly decreases upon oxidation, which is also reflected in the greater deviation from the ideal planarity in the oxidized states (Table S25). In contrast, no change in electron delocalization was detected for the oxidized COT core of the tetramers, most likely due to the persistent nonplanarity of these systems. Nevertheless, formally, a planar COT^{2+} ring should exhibit aromaticity, which manifests in the tendency toward greater planarization upon oxidation as was reproduced by the calculated molecular planarity parameters.[73] Hence, these findings suggest a qualitatively less decrease in aromaticity in the tetraindoles due to the nature of the COT core, as yet another key distinction between the trimeric and tetrameric model species.

In the galvanostatic H-cell cycling shown in Figure 4b, both **sCOT** (yellow) and **aCOT** (green) underwent $2e^-$ charge−discharge cycling at potentials consistent with the first and second oxidation potentials observed in the CV data. Compound **sCOT** displayed a 0.724% fade/h over 100 cycles (∼37.6 h), indicating a moderately high stability for both $\mathbf{sCOT}^{\bullet+}$ and $\mathbf{sCOT}^{2+}$ on a long-term cycling time scale. Moreover, cycling occurred at around 70% of the theoretical capacity with ∼99% Coulombic efficiency throughout the experiment. Postcycling CV (Figure 4c) and charge−discharge curves (Figure 4d) showed a retention of around 73% of the original capacity after 100 cycles. Despite possessing a high symmetry with only 1,3-arrangements of the indole-N atoms as is disfavored by the regioisomeric engineering strategy, the exceptional cycling stability can again be attributed to the reduced loss in aromaticity upon $2e^-$ oxidation as an additional charge stabilization mechanism. This aromaticity effect is also reflected in the calculated spin density distributions (Figure 5a), indicating greater spin localization in the inner 8π core ring of the tetraindoles compared to the triindoles, thereby better shielding the excess spin from degradative intermolecular interactions (Figure 5b and Table S29). Although the concept of utilizing relief of antiaromaticity or reduced loss of global aromaticity in nonaromatic or antiaromatic compounds has previously been leveraged to design multielectron solid batteries[74−77] and other functional organic materials[78−80] or even control reactivity,[81−83] it has not yet been explored in a static H-cell or flow battery context in the literature.

Compared to **sCOT**, **aCOT** displayed an even higher electrochemical cycling stability with only 0.125% capacity fade/h over 100 cycles (∼39.4 h) [Figure 4b (green trace)]. This was achieved while cycling at approximately 73% of the theoretical capacity with ∼99% Coulombic efficiency and a remarkable capacity retention of around 95% of the original capacity.

Postcycling CV [Figure 4e (dotted line)] only displayed slight decomposition of **aCOT**, and the charge−discharge curves (Figure 4f) showed almost no change in discharge capacity over 100 cycles, further confirming the exceptionally high stability of both $\mathbf{aCOT}^{\bullet+}$ and $\mathbf{aCOT}^{2+}$. Similar to the effect of regioisomeric engineering on the triindoles, DFT calculations revealed that upon engineering the regioisomerism of the tetraindoles from $\mathbf{sCOT\text{-}NMe}^{\bullet+}$ to $\mathbf{aCOT\text{-}NMe}^{\bullet+}$, the spin density shifted from the outer and middle carbon atoms to the NMe moieties, resulting in a lower peripheral-to-core ratio for spin localization. This is again accompanied by a transfer of fractional positive charge from the middle carbon atoms to the NMe subunit, for both the mono and dications (see Section X of the Supporting Information for all charge and spin distribution data). Although π-resonance stabilization interactions, fundamental to the regioisomeric engineering strategy, are sensitive to geometric distortions within the conjugated system, the experimental and computational findings above demonstrate the effectiveness of this strategy in stabilizing charged radicals and multicharged species and improving cycling stability also in nonplanar systems. Therefore, the combination of charge and spin stabilization from regioisomeric engineering and reduced loss of aromaticity upon oxidation engenders **aCOT** with exceptionally high cycling stability, ranking at the top among the tested **SCT**, **ACT**, **sCOT**, and **aCOT**.

Comparing Multicharge and Spin Stabilization in the Triindole and Tetraindole Systems. The order of cycling stability for the four compounds is as follows: **aCOT** (0.125% fade/h) > **sCOT** (0.724% fade/h) > **ACT** (1.01% fade/h) > **SCT** (decomposition). Therefore, the more operative the stabilization mechanisms (e.g., regioisomeric engineering and reduced aromaticity loss), the higher the stability of the charged species and thus cycling stability. The additive effect of the charge and spin stabilization mechanisms is also evident in the stepwise redistribution of spin density as calculated by DFT. Building upon the increased spin localization in the core ring due to the influence of aromaticity, spin density is subsequentially further shifted to the NMe moieties upon regioisomeric engineering, eventually resulting in an even lower peripheral-to-core ratio for spin localization in $\mathbf{aCOT\text{-}NMe}^{\bullet+}$ (Figures 5b and S29).

Tetraindoles generally exhibit much higher cycling stabilities than triindoles with analogous symmetry (e.g., the stability of **aCOT** > **ACT** and **sCOT** > **SCT**). This observation highlights the role of the change in aromaticity upon $2e^-$ oxidation as an additional charge stabilization mechanism. Nevertheless, regioisomeric engineering remains effective in both near-planar triindoles and nonplanar tetraindoles; however, the impact of this strategy is more pronounced in near-planar triindoles where π-conjugation is more efficient compared to the nonplanar tetraindoles, for which π-conjugation is less efficient due to the tub-shaped geometry. This trend is also reflected in the results of the TCS analysis for the tetraindoles (see Figures 5c and S47), which only revealed minor differences between the high- and low-symmetry forms and are less consistent overall as the TCS analysis appears to be affected by the nonplanarity of the tetraindoles (see Supporting Information for a detailed discussion). Nevertheless, we believe that evaluating the TCS rule[61,62] in combination with a charge and spin density redistribution analysis offers a computationally simple yet qualitatively insightful methodology for assessing the relative stabilities of regioisomers in near-planar π-systems for optimal battery design, albeit quantitative predictions are not possible. For instance, DFT calculations for the remaining positional isomers of **sCOT** and **aCOT** with more 1,2- and 1,4-arrangements of the indole-N donors suggest similar or even better peripheral-to-core spin density ratios and heteroatom charge stabilization (Tables S26 and S29), rendering these molecules promising candidates for future performance studies.

Deployment in Flow Battery. Mass transport and electrokinetics of the triindoles and tetraindoles catholytes, as measured by diffusion coefficients and electron transfer rates, respectively (see the Supporting Information for complete details), were all in the range of reported $2e^-$ organic catholytes.[24,33,84−87] Therefore, the flow battery performance

https://doi.org/10.1021/jacs.4c16027
J. Am. Chem. Soc. 2025, 147, 2115−2128

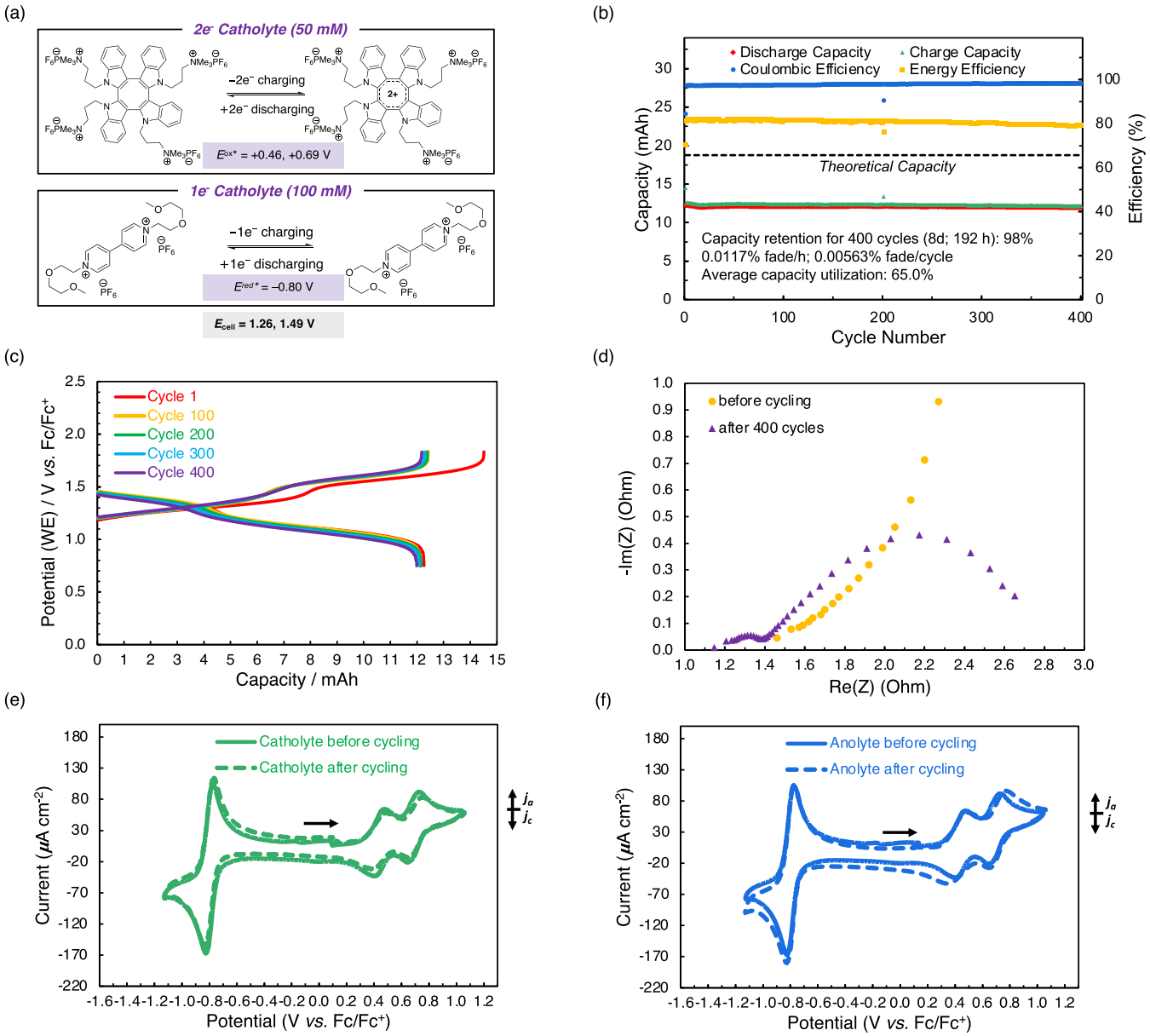

Figure 6. (a) Catholyte and anolyte electrochemical reactions in the flow battery of 50 mM **aCOT-C3N** (**4b**) and 100 mM **2OPEGV(PF$_6$)$_2$** (**5**). (b) Charge capacity, discharge capacity, Coulombic efficiency, and energy efficiency versus the cycle number of flow battery cycling of mixed solution of 50 mM **aCOT-C3N** (**4b**) and 100 mM **2OPEGV(PF$_6$)$_2$** (**5**). (c) Potential versus capacity for cycles 1, 100, 200, 300, and 400 of flow battery cycling of 50 mM **aCOT-C3N** (**4b**) and 100 mM **2OPEGV(PF$_6$)$_2$** (**5**). (d) Electrochemical impedance spectroscopy on the flow battery cell before and after 400 cycles. Precycling (solid line) and postcycling (dotted line) CVs of the (e) catholyte and (f) anolyte in the flow battery cycling of mixed solution of 50 mM **aCOT-C3N** (**4b**) and 100 mM **2OPEGV(PF$_6$)$_2$** (**5**) [CV: 5 mM catholyte, 0.5 M TBAPF$_6$/MeCN solution, scan rate = 100 mV/s, glassy carbon working electrode, Pt counter, Ag/Ag$^+$ (10 mM AgBF$_4$), and N$_2$ glovebox] (flow battery cycling: 0.5 M TBAPF$_6$/MeCN, carbon felt electrodes, FAPQ-330 anionic-exchange membrane, 20 mA/cm^2, flow rate = 20 mL/min, upper voltage cutoff = 1.83 V, and lower voltage cutoff = 0.75 V) (see the Supporting Information for details of the flow battery setup).

of these molecules was set to be further examined. Compared to charge−discharge cycling in a static H-cell, full-flow battery cycling is more challenging since it opens up new decomposition pathways in various aspects.[24] Among the tested compounds, **aCOT** emerged as the best 2e$^-$ catholyte, demonstrating remarkable H-cell cycling stability with a minimal capacity fade of 0.125% fade/h. Consequently, it was chosen for further optimization and investigation in the flow battery setup. Upon changing the side chains from the neutral PEG chain to alkyl-tethered cationic ammonium salts, **aCOT-C3N** displayed two reversible oxidation waves at +0.46 V and +0.69 V vs Fc/Fc$^+$ at higher potentials than **aCOT** ($E_{1/2}^{ox}$: +0.32 and +0.59 V vs Fc/Fc$^+$), while displaying 0.288% fade/h [Figure S11(2)]. With the aim of optimizing the V_{cell} of the flow battery, **aCOT-C3N** was selected as the 2e$^-$ catholyte. As for the anolyte, the 1e$^-$ anolyte PEG-tethered viologen **2OPEGV(PF$_6$)$_2$** ($E_{1/2}^{red1}$: −0.80 V vs Fc/Fc$^+$) was selected due to its proven stability in single-electron flow battery cycling in organic solvents and its high compatibility with various multielectron organic catholytes.[14,16,28]

The flow battery was constructed with a mixed solution of 50 mM **aCOT-C3N** as the 2e$^-$ catholyte and 100 mM **2OPEGV-(PF$_6$)$_2$** as the 1e$^-$ anolyte in 0.5 M TBAPF$_6$/MeCN, which were added in equal volumes (7.0 mL) to the catholyte and anolyte reservoirs. This constitutes a theoretical V_{cell} of 1.26 V for the

https://doi.org/10.1021/jacs.4c16027
J. Am. Chem. Soc. 2025, 147, 2115−2128

inner redox couple and 1.49 V for the outer redox couple. The electrolyte solutions were charged and discharged at a constant current density of 20 mA/cm^2 until cutoff voltages of 1.83 V (+340 mV from the outer redox couple for charging) and 0.75 V (−510 mV from the inner redox couple for discharging) were reached at a 20 mL/min flow rate. The cell was separated by a FAPQ-330 anionic-exchange membrane. The electrochemical reaction during the charge−discharge process for the flow battery system is depicted in Figure 6a (Supporting Information Sections IV and VII for complete details of the flow battery setup), and the flow battery was tested for 400 cycles (∼192 h; ∼8 d) (Figure 6b).

The initial capacity utilization reached ∼65%, while the average energy efficiency was ∼81% with an average Coulombic efficiency of 98%. After the first 100 cycles (∼48 h), the capacity fade was 0.0224% and 0.0108% fade/cycle, with 99% of the original capacity retained. After 200 cycles (∼96 h), the capacity fade was 0.00945% fade/h and 0.00455% fade/cycle, with 99% of the original capacity retained. After 300 cycles, the capacity fade was 0.0103% fade/h and 0.00498% fade/cycle, still with 99% of the original capacity retained. Finally after 400 cycles, the capacity fade was 0.0117% fade/h and 0.00563% fade/cycle, with 98% of the original capacity retained. The minimal capacity loss over the course of 400 cycles of flow battery operation is consistent with the almost identical charge−discharge curves after the first charging event (Figure 6c) and the absence of new peaks or significant amplitude decrease in the postcycling CVs of both the catholyte (Figure 6e) and anolyte (Figure 6f). This flow battery exhibits the highest capacity retention ever reported over 400 cycles in a multielectron all-organic flow battery setup. Consequently, this shows the effectiveness of the two charge stabilization mechanisms in cycling stability enhancement in a proof-of-principle flow battery setup.

■ CONCLUSIONS

In this work, we report that regioisomeric engineering enhances the stability of the charged species and hence the cycling stability of two new classes of 2e$^-$ catholytes, including aromatic near-planar cyclic triindoles and nonaromatic nonplanar cyclic tetraindoles, by increasing the number of ortho- (or 1,2) or para- (or 1,4) arrangements and thus resonance stabilization interactions of the indole nitrogen atoms around the core ring. This charge and spin stabilization mechanism complements the classical donor-incorporation strategy by redistributing the charge and spin densities, thereby also circumventing substituent-induced decomposition pathways. Reduced loss of aromaticity in COTs upon 2e$^-$ oxidation serves as an additional charge stabilization mechanism, as shown in the generally higher stability of cyclic tetraindoles compared to the cyclic triindoles. DFT calculations further revealed that the enhanced cycling stability arising from symmetry breaking and reduced aromaticity loss upon oxidation is accompanied by a spin density shift from the peripheral benzene-C atoms to the indole-N atoms and the inner core ring, respectively, which is generalized by a lower peripheral-to-core ratio for spin localization. Lastly, **aCOT-C3N**, an asymmetrical nonaromatic 2e$^-$ catholyte candidate with an optimized oxidation potential, was paired with PEG-viologen and deployed in a proof-of-principle all-organic flow battery with 1.26−1.49 V, 98% average Coulombic efficiency, 81% average energy efficiency, and only 0.0117% fade/h and 0.00563% fade/cycle over 400 cycles (192 h, ∼8 d), which is the highest capacity retention ever recorded over 400 cycles in a multielectron all-organic flow battery setup. In summary, we anticipate that regioisomeric engineering, which may be charge-independent and is complementary to conventional electronic and steric approaches, may also be applicable in multicharge and spin stabilization in other functional organic materials.

■ ASSOCIATED CONTENT

Supporting Information

The Supporting Information is available free of charge at https://pubs.acs.org/doi/10.1021/jacs.4c16027.

Experimental procedures, compound characterization, additional computational data, discussion of the reliability of the DFT results, and computational details (PDF)

Calculated coordinates of the investigated structures (ZIP)

■ AUTHOR INFORMATION

Corresponding Author

F. Dean Toste − *Department of Chemistry, University of California, Berkeley, California 94720, United States; Chemical Science Division, Lawrence Berkeley National Laboratory, Berkeley, California 94720, United States; Joint Center for Energy Storage Research (JCESR), Argonne, Illinois 60439, United States;* orcid.org/0000-0001-8018-2198; Email: fdtoste@berkeley.edu

Authors

H. T. Katie Chung − *Department of Chemistry, University of California, Berkeley, California 94720, United States; Chemical Science Division, Lawrence Berkeley National Laboratory, Berkeley, California 94720, United States; Joint Center for Energy Storage Research (JCESR), Argonne, Illinois 60439, United States*

Tim K. Schramm − *Department of Chemistry, University of California, Berkeley, California 94720, United States; Department of Chemistry, RWTH Aachen University, Aachen 52074, Germany;* orcid.org/0000-0003-3196-6273

Martin Head-Gordon − *Department of Chemistry, University of California, Berkeley, California 94720, United States; Chemical Science Division, Lawrence Berkeley National Laboratory, Berkeley, California 94720, United States;* orcid.org/0000-0002-4309-6669

James Shee − *Department of Chemistry, Rice University, Houston, Texas 77005, United States;* orcid.org/0000-0001-8333-8151

Complete contact information is available at: https://pubs.acs.org/10.1021/jacs.4c16027

Author Contributions

M.H-G. is a part-owner of Q-Chem Inc., whose software was used for the calculations reported herein.

Notes

The authors declare no competing financial interest.

■ ACKNOWLEDGMENTS

This work is supported by the Joint Center for Energy Storage Research (JCESR), a Department of Energy, Energy Innovation Hub. H.T.K.C. acknowledges financial support from the Croucher Foundation and helpful discussions with Dr. Jacob S. Tracy, Dr. Sai Ho Pun, and Dr. Wenhao Zhang. T.K.S. acknowledges generous financial support from the German Academic Scholarship Foundation and thanks Prof. Christoph

Bannwarth for fruitful discussions as well as preliminary *hh*-TDA calculations. T.K.S. further thanks Dr. Dennis Milešević for critical feedback on the manuscript. M.H.-G. acknowledges funding by the National Institutes of Health and the U.S. National Science Foundation through grant nos. 5U01GM121667 and CHE-1955643. We thank Dr. Hasan Celik, Dr. Raynald Giovine, and Pines Magnetic Resonance Center's Core NMR Facility (PMRC Core) for spectroscopic assistance. The instrument used in this work was in part supported by NIH S10OD024998. We would like to thank Dr. Gan Chen for generously providing us with the FAPQ-330 membrane.

■ REFERENCES

(1) Tang, B.; Zhao, J.; Xu, J. F.; Zhang, X. Tuning the stability of organic radicals: from covalent approaches to non-covalent approaches. *Chem. Sci.* **2020**, *11* (5), 1192−1204.

(2) Kato, K.; Osuka, A. Platforms for Stable Carbon-Centered Radicals. *Angew. Chem., Int. Ed.* **2019**, *58* (27), 8978−8986.

(3) Hicks, R. *Stable Radicals: Fundamentals and Applied Aspects of Odd-Electron Compounds*; John Wiley & Sons, Inc.: United Kingdom, 2010.

(4) Alotto, P.; Guarnieri, M.; Moro, F. Redox flow batteries for the storage of renewable energy: A review. *Renewable Sustainable Energy Rev.* **2014**, *29*, 325−335.

(5) Dunn, B.; Kamath, H.; Tarascon, J.-M. Electrical Energy Storage for the Grid: A Battery of Choices. *Science* **2011**, *334* (6058), 928−935.

(6) Rugolo, J.; Aziz, M. J. Electricity storage for intermittent renewable sources. *Energy Environ. Sci.* **2012**, *5* (5), 7151.

(7) Sánchez-Díez, E.; Ventosa, E.; Guarnieri, M.; Trovò, A.; Flox, C.; Marcilla, R.; Soavi, F.; Mazur, P.; Aranzabe, E.; Ferret, R. Redox flow batteries: Status and perspective towards sustainable stationary energy storage. *J. Power Sources* **2021**, *481*, 228804.

(8) Soloveichik, G. L. Flow Batteries: Current Status and Trends. *Chem. Rev.* **2015**, *115* (20), 11533−11558.

(9) Wei, X.; Cosimbescu, L.; Xu, W.; Hu, J. Z.; Vijayakumar, M.; Feng, J.; Hu, M. Y.; Deng, X.; Xiao, J.; Liu, J.; Sprenkle, V.; Wang, W. Towards High-Performance Nonaqueous Redox Flow Electrolyte Via Ionic Modification of Active Species. *Adv. Energy Mater.* **2014**, *5* (1), 1400678.

(10) Li, Z.; Li, S.; Liu, S.; Huang, K.; Fang, D.; Wang, F.; Peng, S. Electrochemical Properties of an All-Organic Redox Flow Battery Using 2,2,6,6-Tetramethyl-1-Piperidinyloxy and N-Methylphthalimide. *Electrochem. Solid-State Lett.* **2011**, *14* (12), A171−A173.

(11) Huang, J.; Cheng, L.; Assary, R. S.; Wang, P.; Xue, Z.; Burrell, A. K.; Curtiss, L. A.; Zhang, L. Liquid Catholyte Molecules for Nonaqueous Redox Flow Batteries. *Adv. Energy Mater.* **2014**, *5* (6), 1401782.

(12) Milshtein, J. D.; Kaur, A. P.; Casselman, M. D.; Kowalski, J. A.; Modekrutti, S.; Zhang, P. L.; Harsha Attanayake, N.; Elliott, C. F.; Parkin, S. R.; Risko, C.; Brushett, F. R.; Odom, S. A. High current density, long duration cycling of soluble organic active species for non-aqueous redox flow batteries. *Energy Environ. Sci.* **2016**, *9* (11), 3531−3543.

(13) Sevov, C. S.; Samaroo, S. K.; Sanford, M. S. Cyclopropenium Salts as Cyclable, High-Potential Catholytes in Nonaqueous Media. *Adv. Energy Mater.* **2016**, *7* (5), 1602027.

(14) Yan, Y.; Vaid, T. P.; Sanford, M. S. Bis(diisopropylamino)-cyclopropenium-arene Cations as High Oxidation Potential and High Stability Catholytes for Non-aqueous Redox Flow Batteries. *J. Am. Chem. Soc.* **2020**, *142* (41), 17564−17571.

(15) Yan, Y.; Robinson, S. G.; Sigman, M. S.; Sanford, M. S. Mechanism-Based Design of a High-Potential Catholyte Enables a 3.2 V All-Organic Nonaqueous Redox Flow Battery. *J. Am. Chem. Soc.* **2019**, *141* (38), 15301−15306.

(16) Yan, Y.; Walser-Kuntz, R.; Sanford, M. S. Targeted Optimization of Phenoxazine Redox Center for Nonaqueous Redox Flow Batteries. *ACS Mater. Lett.* **2022**, *4* (4), 733−739.

(17) Wei, X.; Xu, W.; Huang, J.; Zhang, L.; Walter, E.; Lawrence, C.; Vijayakumar, M.; Henderson, W. A.; Liu, T.; Cosimbescu, L.; Li, B.; Sprenkle, V.; Wang, W. Radical Compatibility with Nonaqueous Electrolytes and Its Impact on an All-Organic Redox Flow Battery. *Angew. Chem., Int. Ed.* **2015**, *54* (30), 8684−8687.

(18) Sevov, C. S.; Brooner, R. E.; Chenard, E.; Assary, R. S.; Moore, J. S.; Rodriguez-Lopez, J.; Sanford, M. S. Evolutionary Design of Low Molecular Weight Organic Anolyte Materials for Applications in Nonaqueous Redox Flow Batteries. *J. Am. Chem. Soc.* **2015**, *137* (45), 14465−14472.

(19) Sevov, C. S.; Hickey, D. P.; Cook, M. E.; Robinson, S. G.; Barnett, S.; Minteer, S. D.; Sigman, M. S.; Sanford, M. S. Physical Organic Approach to Persistent, Cyclable, Low-Potential Electrolytes for Flow Battery Applications. *J. Am. Chem. Soc.* **2017**, *139* (8), 2924−2927.

(20) Zhang, C.; Niu, Z.; Ding, Y.; Zhang, L.; Zhou, Y.; Guo, X.; Zhang, X.; Zhao, Y.; Yu, G. Highly Concentrated Phthalimide-Based Anolytes for Organic Redox Flow Batteries with Enhanced Reversibility. *Chem* **2018**, *4* (12), 2814−2825.

(21) Huang, J.; Duan, W.; Zhang, J.; Shkrob, I. A.; Assary, R. S.; Pan, B.; Liao, C.; Zhang, Z.; Wei, X.; Zhang, L. Substituted thiadiazoles as energy-rich anolytes for nonaqueous redox flow cells. *J. Mater. Chem. A* **2018**, *6* (15), 6251−6254.

(22) Yan, Y.; Zhang, L.; Walser-Kuntz, R.; Vogt, D. B.; Sigman, M. S.; Yu, G.; Sanford, M. S. Benzotriazoles as Low-Potential Anolytes for Non-aqueous Redox Flow Batteries. *Chem. Mater.* **2022**, *34* (23), 10594−10605.

(23) Zhang, W.; Walser-Kuntz, R.; Tracy, J. S.; Schramm, T. K.; Shee, J.; Head-Gordon, M.; Chen, G.; Helms, B. A.; Sanford, M. S.; Toste, F. D. Indolo[2,3-b]quinoxaline as a Low Reduction Potential and High Stability Anolyte Scaffold for Nonaqueous Redox Flow Batteries. *J. Am. Chem. Soc.* **2023**, *145* (34), 18877−18887.

(24) Yan, Y.; Robinson, S. G.; Vaid, T. P.; Sigman, M. S.; Sanford, M. S. Simultaneously Enhancing the Redox Potential and Stability of Multi-Redox Organic Catholytes by Incorporating Cyclopropenium Substituents. *J. Am. Chem. Soc.* **2021**, *143* (33), 13450−13459.

(25) Huang, J.; Yang, Z.; Vijayakumar, M.; Duan, W.; Hollas, A.; Pan, B.; Wang, W.; Wei, X.; Zhang, L. A Two-Electron Storage Nonaqueous Organic Redox Flow Battery. *Adv. Sustainable Syst.* **2018**, *2* (3), 1700131.

(26) Griffin, J. D.; Pancoast, A. R.; Sigman, M. S. Interrogation of 2,2'-Bipyrimidines as Low-Potential Two-Electron Electrolytes. *J. Am. Chem. Soc.* **2021**, *143* (2), 992−1004.

(27) Hendriks, K. H.; Sevov, C. S.; Cook, M. E.; Sanford, M. S. Multielectron Cycling of a Low-Potential Anolyte in Alkali Metal Electrolytes for Nonaqueous Redox Flow Batteries. *ACS Energy Lett.* **2017**, *2* (10), 2430−2435.

(28) Hu, B.; Liu, T. L. Two electron utilization of methyl viologen anolyte in nonaqueous organic redox flow battery. *J. Energy Chem.* **2018**, *27* (5), 1326−1332.

(29) Kowalski, J. A.; Casselman, M. D.; Kaur, A. P.; Milshtein, J. D.; Elliott, C. F.; Modekrutti, S.; Attanayake, N. H.; Zhang, N.; Parkin, S. R.; Risko, C.; Brushett, F. R.; Odom, S. A. A stable two-electron-donating phenothiazine for application in nonaqueous redox flow batteries. *J. Mater. Chem. A* **2017**, *5* (46), 24371−24379.

(30) Kwon, G.; Lee, K.; Lee, M. H.; Lee, B.; Lee, S.; Jung, S.-K.; Ku, K.; Kim, J.; Park, S. Y.; Kwon, J. E.; Kang, K. Bio-inspired Molecular Redesign of a Multi-redox Catholyte for High-Energy Non-aqueous Organic Redox Flow Batteries. *Chem* **2019**, *5* (10), 2642−2656.

(31) Yan, Y.; Vogt, D. B.; Vaid, T. P.; Sigman, M. S.; Sanford, M. S. Development of High Energy Density Diaminocyclopropenium-Phenothiazine Hybrid Catholytes for Non-Aqueous Redox Flow Batteries. *Angew. Chem., Int. Ed.* **2021**, *60* (52), 27039−27045.

(32) Daub, N.; Janssen, R. A. J.; Hendriks, K. H. Imide-Based Multielectron Anolytes as High-Performance Materials in Nonaqueous Redox Flow Batteries. *ACS Appl. Energy Mater.* **2021**, *4* (9), 9248−9257.

(33) Attanayake, N. H.; Kowalski, J. A.; Greco, K. V.; Casselman, M. D.; Milshtein, J. D.; Chapman, S. J.; Parkin, S. R.; Brushett, F. R.; Odom, S. A. Tailoring Two-Electron-Donating Phenothiazines To Enable

https://doi.org/10.1021/jacs.4c16027
J. Am. Chem. Soc. 2025, 147, 2115−2128

High-Concentration Redox Electrolytes for Use in Nonaqueous Redox Flow Batteries. *Chem. Mater.* **2019**, *31* (12), 4353−4363.
(34) Ding, Y.; Zhang, C.; Zhang, L.; Zhou, Y.; Yu, G. Molecular engineering of organic electroactive materials for redox flow batteries. *Chem. Soc. Rev.* **2018**, *47* (1), 69−103.
(35) Hicks, R. G. What's new in stable radical chemistry? *Org. Biomol. Chem.* **2006**, *5* (9), 1321−1338.
(36) Tracy, J. S.; Horst, E. S.; Roytman, V. A.; Toste, F. D. Development of high-voltage bipolar redox-active organic molecules through the electronic coupling of catholyte and anolyte structures. *Chem. Sci.* **2022**, *13* (36), 10806−10814.
(37) Li, X.; Gao, P.; Lai, Y.-Y.; Bazak, J. D.; Hollas, A.; Lin, H.-Y.; Murugesan, V.; Zhang, S.; Cheng, C.-F.; Tung, W.-Y.; Lai, Y.-T.; Feng, R.; Wang, J.; Wang, C.-L.; Wang, W.; Zhu, Y. Symmetry-breaking design of an organic iron complex catholyte for a long cyclability aqueous organic redox flow battery. *Nat. Energy* **2021**, *6* (9), 873−881.
(38) Hu, M.; Wu, W.; Luo, J.; Liu, T. L. Desymmetrization of Viologen Anolytes Empowering Energy Dense, Ultra Stable Flow Batteries toward Long-Duration Energy Storage. *Adv. Energy Mater.* **2022**, *12* (41), 2202085.
(39) Wang, X.; Gautam, R. K.; Jiang, J. J. Strategies for Improving Solubility of Redox-Active Organic Species in Aqueous Redox Flow Batteries: A Review. *Batteries Supercaps* **2022**, *5* (11), No. e202200298.
(40) Weng, W.; Tao, Y.; Zhang, Z.; Redfern, P. C.; Curtiss, L. A.; Amine, K. Asymmetric Form of Redox Shuttle Based on 1,4-Di-tert-butyl-2,5-dimethoxybenzene. *J. Electrochem. Soc.* **2013**, *160* (10), A1711−A1715.
(41) Weng, W.; Huang, J.; Shkrob, I. A.; Zhang, L.; Zhang, Z. Redox Shuttles with Axisymmetric Scaffold for Overcharge Protection of Lithium-Ion Batteries. *Adv. Energy Mater.* **2016**, *6* (19), 1600795.
(42) Turner, N. A.; Freeman, M. B.; Pratt, H. D.; Crockett, A. E.; Jones, D. S.; Anstey, M. R.; Anderson, T. M.; Bejger, C. M. Desymmetrized hexasubstituted [3]radialene anions as aqueous organic catholytes for redox flow batteries. *Chem. Commun.* **2020**, *56* (18), 2739−2742.
(43) Huang, J.; Su, L.; Kowalski, J. A.; Barton, J. L.; Ferrandon, M.; Burrell, A. K.; Brushett, F. R.; Zhang, L. A subtractive approach to molecular engineering of dimethoxybenzene-based redox materials for non-aqueous flow batteries. *J. Mater. Chem. A* **2015**, *3*, 14971−14976.
(44) Rohrbach, S.; Smith, A. J.; Pang, J. H.; Poole, D. L.; Tuttle, T.; Chiba, S.; Murphy, J. A. Concerted Nucleophilic Aromatic Substitution Reactions. *Angew. Chem., Int. Ed.* **2019**, *58* (46), 16368−16388.
(45) Artamkina, G. A.; Egorov, M. P.; Beletskaya, I. P. Some Aspects of Anionic Sigma Complexes. *Chem. Rev.* **1982**, *82*, 427−459.
(46) Hollingsworth, C. A.; Seybold, P. G.; Hadad, C. M. Substituent effects on the electronic structure and pKa of benzoic acid. *Int. J. Quantum Chem.* **2002**, *90* (4−5), 1396−1403.
(47) Gross, K. C.; Seybold, P. G. Substituent effects on the physical properties and pKa of phenol. *Int. J. Quantum Chem.* **2001**, *85* (4−5), 569−579.
(48) Reghu, R. R.; Volyniuk, D.; Kostiv, N.; Norvaisa, K.; Grazulevicius, J. V. Symmetry versus asymmetry: Synthesis and studies of benzotriindole-derived carbazoles displaying different electrochemical and optical properties. *Dyes Pigm.* **2016**, *125*, 159−168.
(49) Ruiz, C.; García-Frutos, E. M.; da Silva Filho, D. A.; López Navarrete, J. T.; Ruiz Delgado, M. C.; Gómez-Lor, B. Symmetry Lowering in Triindoles: Impact on the Electronic and Photophysical Properties. *J. Phys. Chem. C* **2014**, *118* (10), 5470−5477.
(50) Ruiz, C.; Monge, A.; Gutierrez-Puebla, E.; Alkorta, I.; Elguero, J.; Navarrete, J. T.; Ruiz Delgado, M. C.; Gomez-Lor, B. Saddle-Shaped Cyclic Indole Tetramers: 3D Electroactive Molecules. *Chem.—Eur. J.* **2016**, *22* (30), 10651−10660.
(51) Wang, F.; Li, X. C.; Lai, W. Y.; Chen, Y.; Huang, W.; Wudl, F. Synthesis and characterization of symmetric cyclooctatetraindoles: exploring the potential as electron-rich skeletons with extended π-systems. *Org. Lett.* **2014**, *16* (11), 2942−2945.
(52) Deng, T.; Yan, W.; Liu, X.; Hu, G.; Xiao, W.; Mao, S.; Lin, J.; Jiao, Y.; Jin, Y. Cu-Catalyzed Radical Addition and Oxidation Cascade: Unsymmetrical Trimerization of Indole to Access Isotriazatruxene. *Org. Lett.* **2022**, *24* (7), 1502−1506.
(53) Prystupa, M.; Sohnel, T.; Sperry, J. Synthetic Studies toward Bisindigotin: Polyheteroaromatic Scaffolds via Skeletal Rearrangements of a Diacetoxytetraindole. *J. Org. Chem.* **2021**, *86* (1), 74−78.
(54) Wang, L.; Fang, Q.; Lu, Q.; Zhang, S. J.; Jin, Y. Y.; Liu, Z. Q. Octupolar (C3 and S4) Symmetric Cyclized Indole Derivatives: Syntheses, Structures, and NLO Properties. *Org. Lett.* **2015**, *17* (17), 4164−4167.
(55) Górski, K.; Mech-Piskorz, J.; Pietraszkiewicz, M. From truxenes to heterotruxenes: playing with heteroatoms and the symmetry of molecules. *New J. Chem.* **2022**, *46* (19), 8939−8966.
(56) Karon, K.; Lapkowski, M. Carbazole electrochemistry: a short review. *J. Solid State Electrochem.* **2015**, *19* (9), 2601−2610.
(57) Hsiao, S.-H.; Lin, S.-W. Electrochemical synthesis of electrochromic polycarbazole films from N-phenyl-3,6-bis(N-carbazolyl)-carbazoles. *Polym. Chem.* **2016**, *7* (1), 198−211.
(58) Bannwarth, C.; Caldeweyher, E.; Ehlert, S.; Hansen, A.; Pracht, P.; Seibert, J.; Spicher, S.; Grimme, S. Extended tight-binding quantum chemistry methods. *Wiley Interdiscip. Rev.: Comput. Mol. Sci.* **2020**, *11* (2), No. e1493.
(59) Neese, F. Software update: The ORCA program system—Version 5.0. *Wiley Interdiscip. Rev.: Comput. Mol. Sci.* **2022**, *12* (5), No. e1606.
(60) Epifanovsky, E.; Gilbert, A. T. B.; Feng, X.; Lee, J.; Mao, Y.; Mardirossian, N.; Pokhilko, P.; White, A. F.; Coons, M. P.; Dempwolff, A. L.; Gan, Z.; Hait, D.; Horn, P. R.; Jacobson, L. D.; Kaliman, I.; Kussmann, J.; Lange, A. W.; Lao, K. U.; Levine, D. S.; Liu, J.; McKenzie, S. C.; Morrison, A. F.; Nanda, K. D.; Plasser, F.; Rehn, D. R.; Vidal, M. L.; You, Z. Q.; Zhu, Y.; Alam, B.; Albrecht, B. J.; Aldossary, A.; Alguire, E.; Andersen, J. H.; Athavale, V.; Barton, D.; Begam, K.; Behn, A.; Bellonzi, N.; Bernard, Y. A.; Berquist, E. J.; Burton, H. G. A.; Carreras, A.; Carter-Fenk, K.; Chakraborty, R.; Chien, A. D.; Closser, K. D.; Cofer-Shabica, V.; Dasgupta, S.; de Wergifosse, M.; Deng, J.; Diedenhofen, M.; Do, H.; Ehlert, S.; Fang, P. T.; Fatehi, S.; Feng, Q.; Friedhoff, T.; Gayvert, J.; Ge, Q.; Gidofalvi, G.; Goldey, M.; Gomes, J.; Gonzalez-Espinoza, C. E.; Gulania, S.; Gunina, A. O.; Hanson-Heine, M. W. D.; Harbach, P. H. P.; Hauser, A.; Herbst, M. F.; Hernandez Vera, M.; Hodecker, M.; Holden, Z. C.; Houck, S.; Huang, X.; Hui, K.; Huynh, B. C.; Ivanov, M.; Jasz, A.; Ji, H.; Jiang, H.; Kaduk, B.; Kahler, S.; Khistyaev, K.; Kim, J.; Kis, G.; Klunzinger, P.; Koczor-Benda, Z.; Koh, J. H.; Kosenkov, D.; Koulias, L.; Kowalczyk, T.; Krauter, C. M.; Kue, K.; Kunitsa, A.; Kus, T.; Ladjanszki, I.; Landau, A.; Lawler, K. V.; Lefrancois, D.; Lehtola, S.; Li, R. R.; Li, Y. P.; Liang, J.; Liebenthal, M.; Lin, H. H.; Lin, Y. S.; Liu, F.; Liu, K. Y.; Loipersberger, M.; Luenser, A.; Manjanath, A.; Manohar, P.; Mansoor, E.; Manzer, S. F.; Mao, S. P.; Marenich, A. V.; Markovich, T.; Mason, S.; Maurer, S. A.; McLaughlin, P. F.; Menger, M.; Mewes, J. M.; Mewes, S. A.; Morgante, P.; Mullinax, J. W.; Oosterbaan, K. J.; Paran, G.; Paul, A. C.; Paul, S. K.; Pavosevic, F.; Pei, Z.; Prager, S.; Proynov, E. I.; Rak, A.; Ramos-Cordoba, E.; Rana, B.; Rask, A. E.; Rettig, A.; Richard, R. M.; Rob, F.; Rossomme, E.; Scheele, T.; Scheurer, M.; Schneider, M.; Sergueev, N.; Sharada, S. M.; Skomorowski, W.; Small, D. W.; Stein, C. J.; Su, Y. C.; Sundstrom, E. J.; Tao, Z.; Thirman, J.; Tornai, G. J.; Tsuchimochi, T.; Tubman, N. M.; Veccham, S. P.; Vydrov, O.; Wenzel, J.; Witte, J.; Yamada, A.; Yao, K.; Yeganeh, S.; Yost, S. R.; Zech, A.; Zhang, I. Y.; Zhang, X.; Zhang, Y.; Zuev, D.; Aspuru-Guzik, A.; Bell, A. T.; Besley, N. A.; Bravaya, K. B.; Brooks, B. R.; Casanova, D.; Chai, J. D.; Coriani, S.; Cramer, C. J.; Cserey, G.; DePrince, A. E., 3rd; DiStasio, R. A., Jr.; Dreuw, A.; Dunietz, B. D.; Furlani, T. R.; Goddard, W. A., 3rd; Hammes-Schiffer, S.; Head-Gordon, T.; Hehre, W. J.; Hsu, C. P.; Jagau, T. C.; Jung, Y.; Klamt, A.; Kong, J.; Lambrecht, D. S.; Liang, W.; Mayhall, N. J.; McCurdy, C. W.; Neaton, J. B.; Ochsenfeld, C.; Parkhill, J. A.; Peverati, R.; Rassolov, V. A.; Shao, Y.; Slipchenko, L. V.; Stauch, T.; Steele, R. P.; Subotnik, J. E.; Thom, A. J. W.; Tkatchenko, A.; Truhlar, D. G.; Van Voorhis, T.; Wesolowski, T. A.; Whaley, K. B.; Woodcock, H. L., 3rd; Zimmerman, P. M.; Faraji, S.; Gill, P. M. W.; Head-Gordon, M.; Herbert, J. M.; Krylov, A. I. Software for the frontiers of quantum chemistry: An

https://doi.org/10.1021/jacs.4c16027
J. Am. Chem. Soc. 2025, 147, 2115−2128

overview of developments in the Q-Chem 5 package. *J. Chem. Phys.* **2021**, *155* (8), 084801.
(61) Gimarc, B. M. Topological Charge Stabilization. *J. Am. Chem. Soc.* **1983**, *105*, 1979−1984.
(62) Aihara, J.-i. Topological Charge Stabilization Rule and Quasi-Aromaticity. *Bull. Chem. Soc. Jpn.* **1987**, *60*, 2268−2270.
(63) Barker, J. E.; Price, T. W.; Karas, L. J.; Kishi, R.; MacMillan, S. N.; Zakharov, L. N.; Gomez-Garcia, C. J.; Wu, J. I.; Nakano, M.; Haley, M. M. A Tale of Two Isomers: Enhanced Antiaromaticity/Diradical Character versus Deleterious Ring-Opening of Benzofuran-fused s-Indacenes and Dicyclopenta[b,g]naphthalenes. *Angew. Chem., Int. Ed.* **2021**, *60* (41), 22385−22392.
(64) Li, Y.; Evans, J. N. S. The Fukui Function: A Key Concept Linking Frontier Molecular Orbital Theory and the Hard-Soft-Acid-Base Principle. *J. Am. Chem. Soc.* **1995**, *117*, 7756−7759.
(65) Chen, Z.; Wannere, C. S.; Corminboeuf, C.; Puchta, R.; Schleyer, P. v. R. Nucleus-Independent Chemical Shifts (NICS) as an Aromaticity Criterion. *Chem. Rev.* **2005**, *105*, 3842−3888.
(66) Schleyer, P. v. R.; Maerker, C.; Dransfeld, A.; Jiao, H.; van Eikema Hommes, N. J. R. Nucleus-Independent Chemical Shifts: A Simple and Efficient Aromaticity Probe. *J. Am. Chem. Soc.* **1996**, *118*, 6317−6318.
(67) Gershoni-Poranne, R.; Stanger, A. Magnetic criteria of aromaticity. *Chem. Soc. Rev.* **2015**, *44* (18), 6597−6615.
(68) Stanger, A. NICS − Past and Present. *Eur. J. Org Chem.* **2020**, *2020* (21), 3120−3127.
(69) Kruszewski, J.; Krygowski, T. M. Definition of Aromaticity Basing on the Harmonic Oscillator Model. *Tetrahedron Lett.* **1972**, *13*, 3839−3842.
(70) Krygowski, T. M.; Szatylowicz, H.; Stasyuk, O. A.; Dominikowska, J.; Palusiak, M. Aromaticity from the viewpoint of molecular geometry: application to planar systems. *Chem. Rev.* **2014**, *114* (12), 6383−6422.
(71) Feixas, F.; Matito, E.; Poater, J.; Sola, M. Quantifying aromaticity with electron delocalisation measures. *Chem. Soc. Rev.* **2015**, *44* (18), 6434−6451.
(72) Matito, E.; Duran, M.; Sola, M. The aromatic fluctuation index (FLU): a new aromaticity index based on electron delocalization. *J. Chem. Phys.* **2005**, *122* (1), 14109.
(73) Lu, T. Simple, reliable, and universal metrics of molecular planarity. *J. Mol. Model.* **2021**, *27* (9), 263.
(74) Shin, J. Y.; Yamada, T.; Yoshikawa, H.; Awaga, K.; Shinokubo, H. An antiaromatic electrode-active material enabling high capacity and stable performance of rechargeable batteries. *Angew. Chem., Int. Ed.* **2014**, *53* (12), 3096−3101.
(75) Eder, S.; Yoo, D. J.; Nogala, W.; Pletzer, M.; Santana Bonilla, A.; White, A. J. P.; Jelfs, K. E.; Heeney, M.; Choi, J. W.; Glocklhofer, F. Switching between Local and Global Aromaticity in a Conjugated Macrocycle for High-Performance Organic Sodium-Ion Battery Anodes. *Angew. Chem., Int. Ed.* **2020**, *59* (31), 12958−12964.
(76) Desmaizieres, G.; Speer, M. E.; Thiede, I.; Gaiser, P.; Perner, V.; Kolek, M.; Bieker, P.; Winter, M.; Esser, B. Dibenzo[a,e]-Cyclooctatetraene-Functionalized Polymers as Potential Battery Electrode Materials. *Macromol. Rapid Commun.* **2021**, *42* (18), No. e2000725.
(77) Ding, B.; Bhosale, M.; Bennett, T. L. R.; Heeney, M.; Plasser, F.; Esser, B.; Glocklhofer, F. Reducing undesired solubility of squarephaneic tetraimide for use as an organic battery electrode material. *Faraday Discuss.* **2024**, *250*, 129−144.
(78) Zhang, R.; Ellern, A.; Winter, A. H. Anti-Aromaticity Relief as an Approach to Stabilize Free Radicals. *Angew. Chem., Int. Ed.* **2021**, *60* (47), 25082−25088.
(79) Murai, M.; Enoki, T.; Yamaguchi, S. Dithienoazepine-Based Near-Infrared Dyes: Janus-Faced Effects of a Thiophene-Fused Structure on Antiaromatic Azepines. *Angew. Chem., Int. Ed.* **2023**, *62* (49), No. e202311445.
(80) Kim, H.; Park, W.; Kim, Y.; Filatov, M.; Choi, C. H.; Lee, D. Relief of excited-state antiaromaticity enables the smallest red emitter. *Nat. Commun.* **2021**, *12* (1), 5409.
(81) Karas, L. J.; Wu, C. H.; Wu, J. I. Barrier-Lowering Effects of Baird Antiaromaticity in Photoinduced Proton-Coupled Electron Transfer (PCET) Reactions. *J. Am. Chem. Soc.* **2021**, *143* (43), 17970−17974.
(82) Slanina, T.; Ayub, R.; Toldo, J.; Sundell, J.; Rabten, W.; Nicaso, M.; Alabugin, I.; Fdez Galvan, I.; Gupta, A. K.; Lindh, R.; Orthaber, A.; Lewis, R. J.; Gronberg, G.; Bergman, J.; Ottosson, H. Impact of Excited-State Antiaromaticity Relief in a Fundamental Benzene Photoreaction Leading to Substituted Bicyclo[3.1.0]hexenes. *J. Am. Chem. Soc.* **2020**, *142* (25), 10942−10954.
(83) Rosenberg, M.; Dahlstrand, C.; Kilsa, K.; Ottosson, H. Excited state aromaticity and antiaromaticity: opportunities for photophysical and photochemical rationalizations. *Chem. Rev.* **2014**, *114* (10), 5379−5425.
(84) Hendriks, K. H.; Robinson, S. G.; Braten, M. N.; Sevov, C. S.; Helms, B. A.; Sigman, M. S.; Minteer, S. D.; Sanford, M. S. High-Performance Oligomeric Catholytes for Effective Macromolecular Separation in Nonaqueous Redox Flow Batteries. *ACS Cent. Sci.* **2018**, *4* (2), 189−196.
(85) Kwon, G.; Lee, S.; Hwang, J.; Shim, H.-S.; Lee, B.; Lee, M. H.; Ko, Y.; Jung, S.-K.; Ku, K.; Hong, J.; Kang, K. Multi-redox Molecule for High-Energy Redox Flow Batteries. *Joule* **2018**, *2* (9), 1771−1782.
(86) Gong, K.; Fang, Q.; Gu, S.; Li, S. F. Y.; Yan, Y. Nonaqueous redox-flow batteries: organic solvents, supporting electrolytes, and redox pairs. *Energy Environ. Sci.* **2015**, *8* (12), 3515−3530.
(87) Wei, X.; Duan, W.; Huang, J.; Zhang, L.; Li, B.; Reed, D.; Xu, W.; Sprenkle, V.; Wang, W. A High-Current, Stable Nonaqueous Organic Redox Flow Battery. *ACS Energy Lett.* **2016**, *1* (4), 705−711.

https://doi.org/10.1021/jacs.4c16027
J. Am. Chem. Soc. 2025, 147, 2115−2128